Stable operation of a self-amplified spontaneous-emission free-electron laser in the extremely ultraviolet region

Tsumoru Shintake, Hitoshi Tanaka,* Toru Hara, Takashi Tanaka, Kazuaki Togawa, Makina Yabashi, Yuji Otake, Yoshihiro Asano, Toru Fukui, Teruaki Hasegawa, Atsushi Higashiya, Naoyasu Hosoda, Takahiro Inagaki, Shinobu Inoue, Yujong Kim,† Masanobu Kitamura,‡ Noritaka Kumagai, Hirokazu Maesaka, Sakuo Matsui, Mitsuru Nagasono, Takashi Ohshima, Tatsuyuki Sakurai, Kenji Tamasaku, Yoshihito Tanaka, Takanori Tanikawa,§ Tadashi Togashi, Shukui Wu, Hideo Kitamura, and Tetsuya Ishikawa

XFEL Project Head Office, RIKEN, Kouto 1-1-1, Sayo, Hyogo 671-5148, Japan

Takao Asaka, Teruhiko Bizen, Shunji Goto, Toko Hirono, Miho Ishii, Hiroaki Kimura, Toshiaki Kobayashi, Takemasa Masuda, Tomohiro Matsushita, Xavier Maréchal, Haruhiko Ohashi, Toru Ohata, Katsutoshi Shirasawa, Tetsuya Takagi,‖ Sunao Takahashi, Masao Takeuchi, Ryotaro Tanaka, Akihiro Yamashita, Kenichi Yanagida, and Chao Zhang

Japan Synchrotron Radiation Research Institute, Kouto 1-1-1, Sayo, Hyogo 671-5198, Japan

(Received 6 February 2009; published 2 July 2009)

We achieved stable operation of a free-electron laser (FEL) based on the self-amplified spontaneous-emission (SASE) scheme at the SPring-8 Compact SASE Source (SCSS) test accelerator in the extremely ultraviolet region. Saturation of the SASE FEL power has been achieved at wavelengths ranging from 50 to 60 nm. The pulse energy has reached ~30 μJ at 60 nm. The observed fluctuation of the pulse energy is about 10% (standard deviation) for several hours, which agrees with the expectation from the SASE theory showing the stable operation of the accelerator. The SASE FEL has been routinely operated to provide photon beams for user experiments over a period of a few weeks. Analysis on the experimental data gave the normalized-slice emittance at the lasing part is around 0.7π mm mrad. This result indicates that the normalized-slice emittance of the initial electron beam, 0.6π mm mrad in a 90% core part, is kept almost unchanged after the bunch compression process with a compression factor of approximately 300. The success of the SCSS test accelerator strongly encourages the realization of a compact XFEL source.

DOI: 10.1103/PhysRevSTAB.12.070701 PACS numbers: 29.20.Ej, 29.27.Eg, 41.60.Cr, 52.59.Sa

I. INTRODUCTION

An x-ray free-electron laser (XFEL), which generates coherent and brilliant x-ray beams with ultrashort pulse duration, will innovate research activities in various fields, such as materials science, molecular biology, catalysis engineering, environmental research, and medical science. The self-amplified spontaneous-emission (SASE) [1] scheme is one of the most promising methods to realize XFELs. Here, the brilliant electron beam is periodically wiggled in the magnetic field of an undulator so as to generate laser radiation through electromagnetic interaction between the electrons and the radiation field. This amplification process is applicable to a wide wavelength region from far infrared even to hard x rays, where the conventional laser configuration that combines an optical cavity resonator and the laser medium cannot be exploited.

In order to realize SASE FEL at angstrom wavelengths, an extremely high brilliance electron beam, i.e., high density and low emittance, is required. Therefore, extensive R&Ds on high performance electron sources have been carried out all over the world. An innovative system of a photocathode rf gun was developed in BNL [2]. In the XFEL projects in Europe [3] and the U.S. [4], the accelerator system has been designed based on the photocathode rf gun and multistage bunch compression, followed by the out-of-vacuum undulators. In these projects, a high-energy (15 to 20 GeV) electron beam is employed for producing FEL radiation in an angstrom wavelength range. A large facility scale with a total length of 2 to 3 km is thus required to accelerate the electron beam.

A reduction of the machine size, however, is essential for widespread distribution of XFEL sources. For this purpose, an idea for a compact SASE XFEL source, which is named the SPring-8 compact SASE source (SCSS) [5,6], was proposed in 2000. The Japanese XFEL facility based on this idea is now under construction at SPring-8 and will

*Electronic address: tanaka@spring8.or.jp
†Present address: Paul Scherrer Institut, 5232 Villigen PSI, Switzerland.
‡Present address: Nichizou Electronics & Control Corporation, Electronics Systems Division, Nishikujyo 5-3-28, Konohana-ku, Osaka 554-0012, Japan.
§Present address: School of Physical Sciences, The Graduate University for Advanced Studies (SOKENDAI), Okazaki 444-8585, Japan.
‖Present address: Japan Atomic Energy Agency, 2-4 Shirane Shirakata, Tokai-mura, Naka-gun, Ibaraki 319-1195, Japan.

be completed in 2011 [7,8]. Here, the use of an in-vacuum shorter-period undulator [9], which produces a higher magnetic field with a smaller magnetic gap by locating the magnets inside vacuum, allows us to realize a compact XFEL machine with a lower-energy accelerator, because the wavelength of the FEL radiation is proportional to the periodic length of undulator magnets and to the inverse square of electron beam energy. Another key technology, higher-gradient accelerator, further enables us to reduce the accelerator length.

Although a reduction of the facility scale gives a significant advantage [10], a new technical challenge was requested for generating and accelerating the extremely high-quality electron beam with a small normalized-slice emittance of less than 1π mm mrad. For this purpose, we proposed to use a thermionic cathode gun [11], which has a stable emission property and a long lifetime compared to photocathode rf guns. In order to make up for its low emission current, a velocity bunching [12] section, which can push the total bunch compression factor up to a few thousands, was added to the injector.

The SCSS test accelerator [13,14] was constructed in 2004–2005 to test the performance of the developed components including the thermionic cathode gun and to investigate the beam quality after the bunch compression of high magnitude. The maximum beam energy of the SCSS test accelerator is designed to be 250 MeV using two C-band 50 MW klystrons and four accelerating structures, which generates radiation in the extremely ultraviolet (EUV) region.

In this paper, we present the SASE FEL performance achieved at the SCSS test accelerator and discuss perspectives of the compact SASE source. In Sec. II, we give an overview of the test accelerator system. We explain the handling of the electron beam in the low-emittance injector, where the space charge force can cause serious emittance growth. In Sec. III, we give an outline of the beam commissioning. We focus on the critical subjects required for achieving continuous saturation of the SASE FEL. We present the achieved lasing performance in Sec. IV and discuss the normalized-slice emittance evaluated by analyzing the experimental lasing data in Sec. V.

II. SCSS TEST ACCELERATOR SYSTEM

Figure 1 shows a schematic representation of the SCSS test accelerator, which is composed of five main parts: a low-emittance injector, a bunch compressor based on a magnetic chicane, a C-band acceleration system, an in-vacuum undulator system, and a photon diagnostic system. The total accelerator length is ~60 m. The beam energy of 250 MeV is determined so that the SASE saturation is achievable at the wavelengths between 50 and 60 nm. The beam current available from the 500-kV thermionic gun is 1 A with 2-μs duration, thus initial charge is about 2 μC. Only one two-thousandth of it (1 nC) is transmitted through a deflector and sent to the following velocity bunching process. After full bunch compression and acceleration, the final bunch charge at the undulators is 0.3 nC with a peak current of about 300 A. The repetition rate of the electron bunch is tunable from 1 to 60 Hz. The accelerator is currently operated by a single bunch mode and there is no microbunch structure. The parameters of the test accelerator are listed in Table I.

A. Low-emittance injector [13,14]

The pulsed thermionic-electron gun (1 in Fig. 1) uses a single-crystal CeB_6 cathode with a diameter of 3 mm [11]. The cathode is buried in a graphite sleeve and heated up to ~1800 K by heat radiation from a graphite heater surrounding the sleeve. A smooth surface of the single crystal and a grid-free structure can generate a homogeneous cylindrical electron beam with a sharp-transverse edge [11]. The theoretical thermal emittance determined by

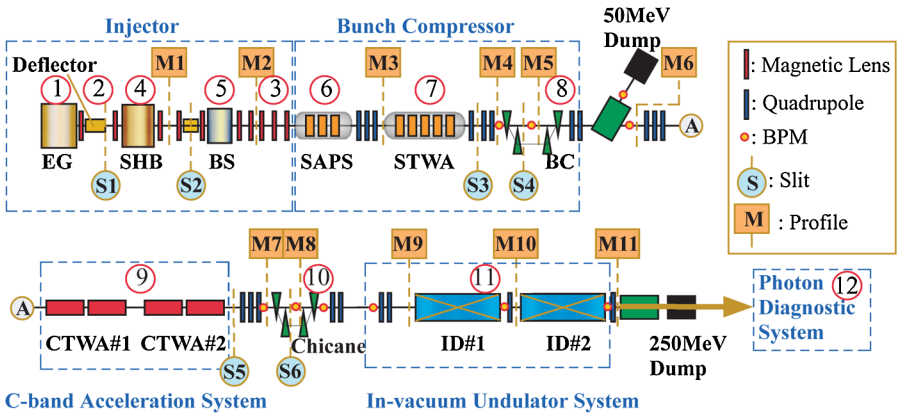

FIG. 1. (Color) Schematic representation of the SCSS test accelerator. 1, 500-kV electron gun (EG); 2, deflector with collimator; 3, a set of ten magnetic lenses; 4, 238-MHz subharmonic buncher (SHB); 5, 476-MHz booster cavity (BS); 6, S-band APS cavity (SAPS); 7, S-band traveling-wave acceleration structure (STWA); 8, bunch compressor (BC); 9, C-band acceleration system (CTWA#1&CTWA#2); 10, chicane; 11, in-vacuum undulator system (ID#1&ID#2); and 12, photon diagnostic system.

TABLE I. Main accelerator parameters.

Electron beam	
Beam energy	250 MeV
Bunch charge	~0.3 nC
Repetition rate	60 Hz (maximum)
Peak current	~300 A
Bunch length	~0.7 ps (FWHM)
Accelerator parameters	
Gun voltage	500 kV
Initial peak current	1 A
Deflector pulse width	1 ns (FWHM)
238 MHz SHB rf voltage amplitude	~200 kV
238 MHz SHB rf phase[a]	−110 deg
476 MHz booster rf voltage amplitude	~700 kV
476 MHz booster rf phase[a]	−25 deg
S-band APS rf voltage amplitude	12 MV
S-band APS rf phase[a]	−24 deg
S-band TWA rf voltage amplitude	38 MV
S-band TWA rf phase[a]	−29 deg
Bunch compressor R_{56}	−20 mm
C-band TWA-1 accelerating gradient	21 MV/m
C-band TWA-1 rf phase[a]	0 deg
C-band TWA-2 accelerating gradient	37 MV/m
C-band TWA-2 rf phase[a]	0 deg
Undulator parameters	
Periodic length	15 mm
Number of periods	300×2
Maximum K	1.5
Minimum/maximum gap	3/25 mm

[a]On-crest phase is the reference.

both the cathode temperature and the size is 0.4π mm mrad when normalized. The deflector (2 in Fig. 1) slices out a 1-ns short pulse from the 2-μs beam extracted from the cathode. In the deflector, a static magnetic field deflects and stops the electron beam. A 2-ns electric pulse with 200-ps rising and falling time generates the electric field, which cancels out the static magnetic field, to pass the 1-ns beam through the deflector. A circular collimator is located right after the deflector, which defines the beam cross section to be cylindrically symmetric with a constant diameter at this fixed location. Thus, this collimator provides a virtual source point of the electron beam optics in the test accelerator.

The initial beam energy of 500 keV, which is higher than that of the conventional gun around 200 keV, sufficiently reduces the space charge effect. The beam envelope evolution by the space charge force can be written by

$$\frac{d^2r}{ds^2} \propto \frac{I}{(\beta\gamma)^3}, \tag{1}$$

where r, s, I, β, and γ represent the beam radius, the longitudinal position, the peak current, the relative velocity, and the relative energy, respectively. By increasing the beam energy from 200 to 500 keV, the beam expanding speed becomes 10 times slower, thus we can remove focusing magnetic fields in the long array of air-core solenoids used in the conventional injector system. Instead, we employed a simple magnetic lens with an iron yoke. Advantages of using this type of magnetic lens are well-defined axisymmetric field profile and small leakage outside the lens [6] (3 in Fig. 1).

The 238-MHz subharmonic buncher (SHB) (4 in Fig. 1) generates a negative energy chirp on the incoming electron beam, which starts a velocity bunching process. At the entrance of the 476-MHz booster cavity (5 in Fig. 1), the average beam energy is 0.43 MeV with a peak current of ~9 A. The booster cavity increases the beam energy up to 1.1 MeV to reduce the space charge effect. The peak current further increases up to ~90 A in the 1.3-m drift section after the booster. Then the electron beam is quickly accelerated to the relativistic energy by the buncher accelerator of an S-band (2856 MHz) alternating-periodic structure (APS) (6 in Fig. 1). A velocity bunching process is terminated at a few cells from the upstream end of the APS and the peak current reaches ~110 A. An advantage of using the APS is its axisymmetric field. Since the power feed coupler is located at the middle of the structure, the entrance cell of the cavity has an axially symmetric geometry without any coupler, where the beam emittance is very sensitive to the field uniformity.

B. Magnetic chicane-based bunch compressor

The S-band acceleration system (6 and 7 in Fig. 1) increases the beam energy up to 45 MeV. The APS and the traveling-wave accelerating (TWA) structure are operated with the bunching phases given in Table I, in order to generate a negative energy chirp over the bunch. The following magnetic chicane (8 in Fig. 1), with a design R_{56} of −20 mm and a maximum horizontal dispersion of 110 mm, compresses the electron bunch by approximately 3 times under the nominal operation condition. The peak current at the exit of the bunch compressor is about 300 A.

C. C-band acceleration system [6]

The C-band (5712 MHz) acceleration system (9 in Fig. 1) [15] was designed to provide a high gradient of 35 MV/m with a maximum repetition rate of 60 Hz. Figure 2 shows a configuration of the C-band accelerator unit [16]. The rf pulse compressor [17] compresses a 2.5-μs rf pulse from the 50-MW klystron [18] into a 0.5-μs short pulse and increases the peak power by 3 times. The 3 dB hybrid coupler divides the compressed rf pulse of 150 MW equally into two and drives the 1.8-m-long TWA structures at a 70-MW peak.

The C-band accelerating structure is composed of 91 cells; the coupling-iris (beam hole) diameters are gradually changed from 17.34 mm at the upstream end to 13.55 mm

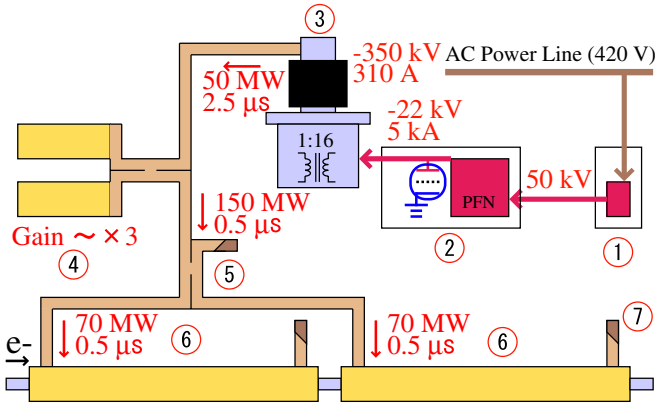

FIG. 2. (Color) Schematic representation of the C-band accelerator unit. The rf power values in the figure are for nominal acceleration gradient of 35 MV/m. 1, inverter high-voltage power supply; 2, compact oil-filled modulator; 3, 50-MW C-band klystron; 4, rf pulse compressor; 5, 3 dB hybrid coupler; 6, choke-mode type accelerating structure; and 7, dummy load.

at the downstream end, which compensates the rf power loss along the structure to provide a quasiconstant accelerating gradient. The acceleration mode is a $3/4\pi$ traveling-wave mode with an averaged shunt impedance of 54 MΩ/m. An accelerating structure with a choke-mode cavity [19], where SiC absorbers damp the excited higher order modes except for the fundamental acceleration mode trapped in the acceleration cavity, was adopted to realize the multibunch operation.

The two C-band units with the four accelerating structures accelerate the beam from 45 to 250 MeV; thus the required acceleration gradient is 29 MV/m, which is lower than the design accelerating gradient of 35 MV/m for the x-ray FEL under construction. In order to investigate machine performance at the maximum accelerating gradient, we performed a high-field test of the C-band acceleration system over a long operation period [20]. In the test, the first and second C-band units were stably operated with different acceleration gradients, 21 and 37 MV/m, respectively, while maintaining an average gradient of 29 MV/m. The dark current emitted from the accelerating structures is removed by the downstream magnetic chicane (10 in Fig. 1).

D. Short-period in-vacuum undulator

According to the numerical simulation, the two in-vacuum undulators (11 in Fig. 1) provide a sufficient amplification gain for achieving SASE saturation at around 60 nm when the ratio of the peak current to the normalized-slice emittance is higher than 400 A/π mm mrad. The required tolerances on the phase and integrated nth multipole errors are 5 deg and 100 Gauss/cm^{n-1}, respectively.

The Halbach configuration with a 45-deg inclined magnetization axis (hereafter, we refer to this configuration as 45-deg inclined Halbach configuration) [21] was adopted for the undulators. In this design, the magnetization axis is inclined by 45 deg as compared to the normal Halbach configuration. Details of adopting the 45-deg inclined Halbach configuration will be found in Ref. [21]. The magnet is made of NdFeB, and the number of periods is 300 per undulator. The undulator gap is tunable between 3 and 25 mm, covering the undulator deflecting parameter, K, from almost zero to 1.5, which can generate the fundamental radiation in wavelengths from 30 to 60 nm with the 250-MeV electron beam. The parameter K is expressed by

$$K = \beta\gamma\theta = 93.4B_0(T) \times \lambda_u(m), \tag{2}$$

where θ, B_0, and λ_u represent the deflection angle per half pole, the peak magnetic field, and the periodic length of undulator magnets, respectively.

In order to compensate the variation of the medium plane level, the upper and lower magnet arrays of the undulator are independently controlled and the height of the undulator can be adjusted within ± 500 μm. Pairs of horizontal and vertical steering magnets are installed at the entrance and exit of each undulator to adjust the beam trajectory over the undulator section. A single quadrupole magnet of horizontal focusing is installed in between the two undulators to maintain a moderate horizontal beam envelope. No quadrupole magnet for vertical focusing is necessary, because of a strong vertical focusing force of the undulators for the 250-MeV electron beam.

E. Photon diagnostic system

Radiation properties are diagnosed with a spectrometer, photodiodes, and fluorescence screens (12 in Fig. 1) [22]. The photon diagnostics system (Fig. 3) is installed downstream of a gold-coated deflecting plane mirror to eliminate background γ rays. The reflectivity of the mirror was calibrated at UVSOR BL5B [23] with an uncertainty of

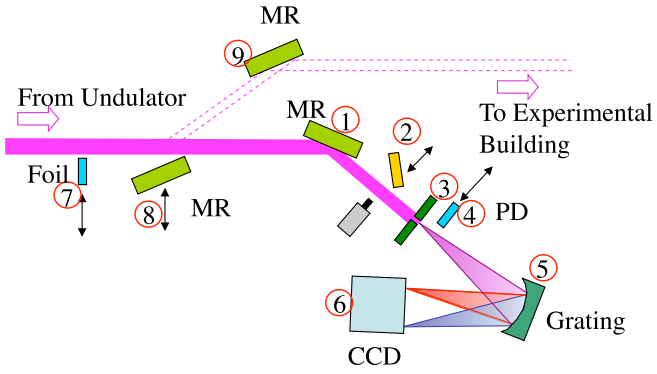

FIG. 3. (Color) Schematic representation of the photon diagnostics system. 1, deflecting plane mirror (MR); 2, fluorescence screen; 3, incident slit; 4, photodiode (PD); 5, concave grating; 6, charge-coupled device (CCD); 7, thin-foil attenuator; 8 and 9, mirrors used for transporting EUV radiation to the experimental building. The double arrow represents a retractable component.

10%. The reflectivity of the mirror is 0.62 to 0.66 in this wavelength range.

The spectrometer is composed of an incident quadrant slit, a gold-coated concave grating (Shimadzu, radius of 922 mm, grating density of 2400 lines/mm), and a charge-coupled device (CCD) camera (Princeton Instruments PI-SX 400, pixel number of 1340×400, pixel size of 20×20 μm). The spectrum of the incident beam is horizontally dispersed onto the CCD plane for single-shot detection. The resolution at 60 nm was designed to be 0.05%.

The pulse energy is measured with a photodiode (IRD SXUV100), which covers a dynamic range of 10^5, which is wide enough for beam tuning by combining a thin-foil attenuator. The efficiency was calibrated at NIST [24] and UVSOR BL5B with an uncertainty of 15%. Thin metal foils are available as attenuators for a high-intensity beam. The transmittance of the foils was calibrated using a spectrometer with an uncertainty of 10%. The total ambiguity in the pulse energy measurement is estimated to be 30%. A supplemental measurement of the pulse energy was performed with the spectrometer. The efficiency was calibrated by comparing the simulated intensity of spontaneous emission with the measured one during the debunching operation. We confirmed that the results from both methods agreed with each other.

III. KEY SUBJECTS FOR ACHIEVING SASE FEL SATURATION

The SCSS test accelerator was completed in March 2006 and the beam tuning was started in May 2006. The first SASE FEL amplification was observed on June 20th. In December 2006, a dummy load (vacuum tube) of the electron gun was broken and the accelerator was shutdown for 6 months. The beam tuning was restarted on June 25, 2007. After reproducing the laser power, we focused on the improvement of the laser stability. At the beginning of September, the magnet array of the second undulator was replaced to increase the SASE FEL amplification gain. At the end of September, we achieved saturation of the SASE FEL power. The net tuning time to the SASE saturation was ten months. The key subjects during the beam tuning are summarized below.

A. Determination of initial conditions at the beam source

In order to determine adequate focusing parameters along the accelerator, the initial conditions (i.e., the angular divergence and the size) of the electron beam from the cathode should be evaluated. The evolution of the electron beam envelope was measured as a function of the strengths of three magnetic lenses [25]. In order to remove chromatic effects, the SHB and the booster cavity were turned off during the measurements, thus all electrons have monochromatic energy at 500 keV.

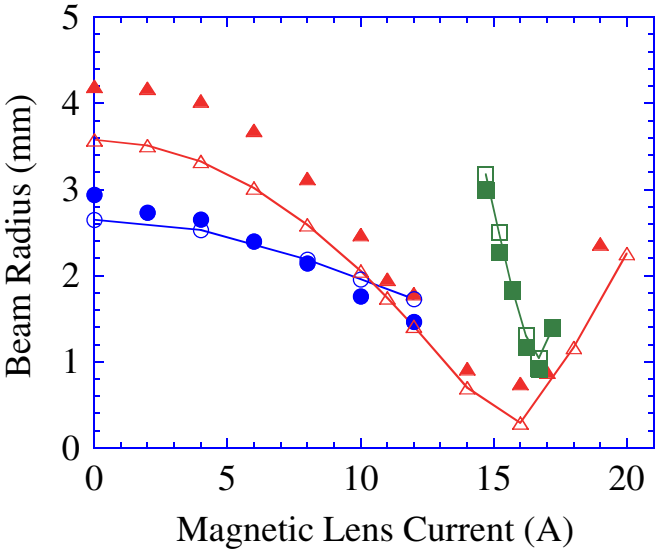

FIG. 4. (Color) Measured beam-size dependences on the magnetic lens strengths compared with the PARMELA code. The filled and open symbols represent measured and numerically fitted data, respectively. The squares show the dependence on the strength of the 1st magnetic lens (ML) at the collimator right after the deflector. The triangles (circles) show the dependence on strength of the 3rd (6th) ML at the 1st (2nd) profile monitor.

The initial conditions of the electron beam were evaluated from the measured data with the following assumptions: (i) a uniform energy distribution and (ii) a cylindrically symmetric distribution with uniform density. Two different calculations were carried out using the PARMELA code and a 2D-cylindrical beam model including the space charge. The results of these calculations agreed well with each other. Figure 4 shows the fitted curves by

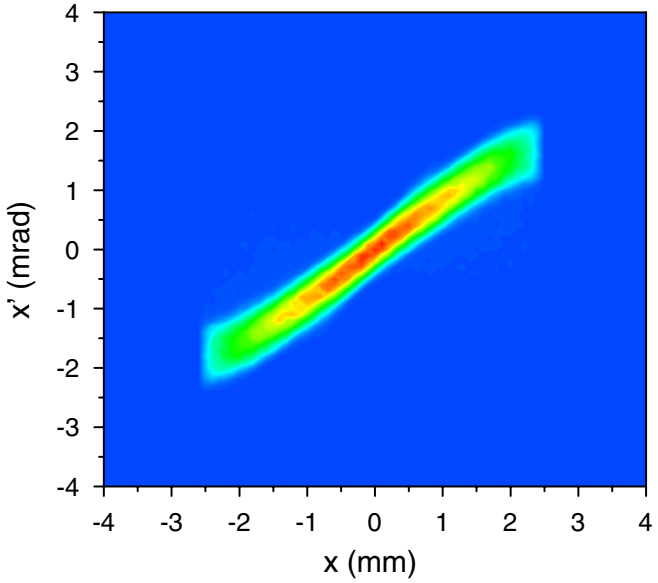

FIG. 5. (Color) Beam distributions in the horizontal phase space simulated using the measurement.

the PARMELA code together with the measured data. Figure 5 is the beam distribution obtained in the simulation at the position of the circular collimator, which provides the virtual source point of the beam optics. This distribution well reproduced the measured distribution in the thermionic-gun performance test [11].

B. Precise parameter setting for velocity bunching with measured bunch-up signals

In the velocity bunching, an upright distribution of the beam in the energy-time phase space gives the minimum bunch length. But we should avoid overbunching to prevent emittance growth. Hence, precise control of the velocity bunching is required. However, the accuracies of the rf amplitude and phase detection are not sufficient.

In order to obtain an adequate parameter set for velocity bunching, we monitored a coherent transition radiation (CTR) signal from a phosphor screen that reflects a temporal profile of the electron bunch. The CTR signal was measured by a microwave spectrometer [26], shown in Fig. 6. This spectrometer can separately detect the CTR intensities of five frequency ranges, which are selected by high-pass filters whose cutoff frequencies are 3.75, 7.5, 15, 30, and 60 GHz.

The three rf parameters (amplitude and phase of the SHB; amplitude of the booster cavity) were preset to the fixed values and the APS was turned off during the measurements. Then, the CTR intensity was measured at the entrance and exit of the APS section as a function of the phase of the booster cavity. Figure 7 shows the measured CTR intensity dependence. The simulated dependence of the peak current defined by a time width of 1 ps was also

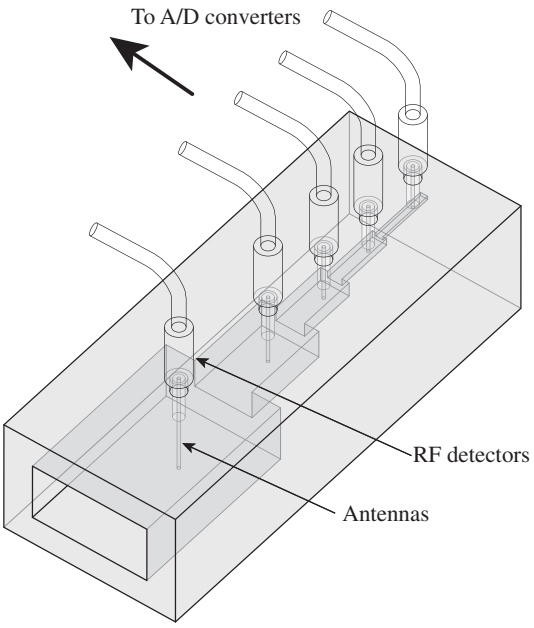

FIG. 6. Schematic representation of the microwave spectrometer.

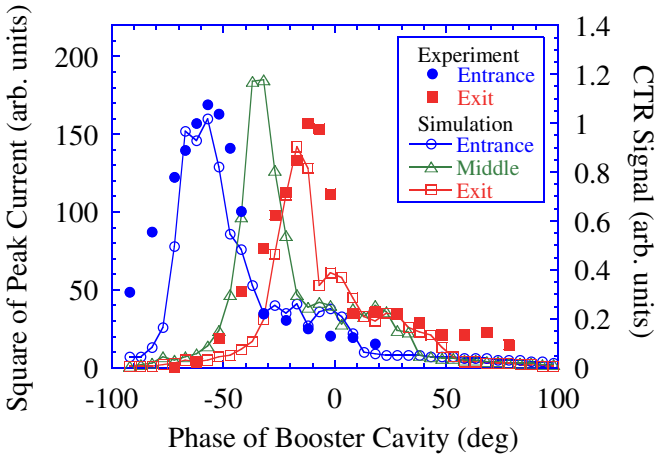

FIG. 7. (Color) Comparison between the measured (filled symbols, $f > 3.75$ GHz) dependence of the CTR intensity on rf phase of the booster cavity and the simulated (open symbols) dependence of the peak current. Squares of the peak current are plotted to reproduce the measured CTR peak shapes. The circles, triangles, and squares represent the entrance, middle, and exit of the APS, respectively.

shown in the figure for the comparison. When the bunch length becomes minimum, the CTR intensity exhibits a peak as shown in Fig. 7. The booster phase giving the minimum bunch length depends on a drift length, because a shorter drift requires a larger energy chirp in the velocity bunching to complete the bunch rotation in the phase space. Since we designed the injector so that the bunch length takes a minimum value at the center of the APS, the phase in the middle of two measured peaks in Fig. 7 gives the design booster phase. When the APS is turned on, the electron velocity bunching is stopped before overbunching due to acceleration. By adjusting the booster phase, the bunch length can be controlled for the SASE FEL operation.

C. Stabilization of injector rf system [27]

The FEL lasing is very sensitive to the electron beam parameters at the lasing slice; therefore, the lasing power is a very useful probe for verifying the beam quality and monitoring machine condition. In order to stabilize the lasing power fluctuation, we investigated the correlations with various machine parameters. We found that the temperature variations of the cooling water supplied to the SHB, the booster, and the APS were the main source of the lasing power fluctuation. Since they are high Q-value resonators, the rf phases are sensitive to the thermal deformation of the cavity body. For example, the phase sensitivity to the temperature variation is ~ 0.01 deg /1 mK for the SHB. We stabilized the temperature of the cavity bodies within 10 mK by improving the control of the cooling water system [28,29]: changing the location of the control points to reduce a response time lag, reoptimiz-

ing the proportional-integral-derivative feedback parameters, and introducing a low-pass filter. By these improvements, the variations of the rf phases and amplitudes have been remarkably reduced by a factor of 2–5.

Slow drifts of the rf phases and amplitudes still remained as perturbation sources even after temperature stabilization. Phase-locked loops and automatic level controls (PLLs and ALCs) with cavity pickup signals were employed to suppress the slow drifts [29]. However, 12-bit digital-to-analog converters in the PLLs and the ALCs severely restricted the setting resolution. For instance, the setting resolution for an rf phase was limited to ~0.09 deg , which was found to be insufficient for achieving the stable lasing. In order to improve the setting resolutions, a waveform dithering method was introduced, which varies a parameter value during the cavity filling time. This modification could effectively improve the resolutions of the integrated parameters. Together with other improvements on the phase/amplitude control algorithm, the effective resolutions were improved by approximately one order [29].

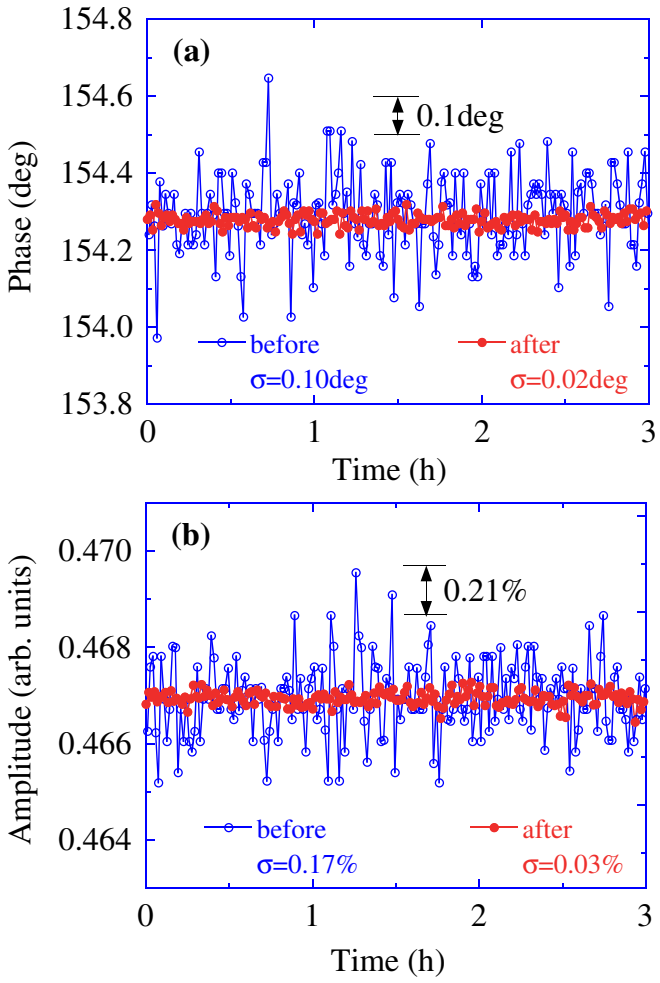

FIG. 8. (Color) Achieved stabilities of the rf phase (a) and the rf amplitude (b) for the SHB over a 3-h period. The open and filled circles represent the stabilities before and after the improvements, respectively.

Figure 8 shows the rf phase and amplitude stabilities of the SHB. After the improvements, the phase and amplitude variations became 0.02 deg and 0.03% in standard deviation (STD), respectively. Sensitivity analysis on the peak current against a variation of each rf parameter shows that the achieved stability gives a peak current fluctuation of ~8% in STD assuming random variations with no correlation. As shown in Sec. V, it is estimated that this peak current fluctuation by the accelerator instability causes a fluctuation of ~10% in the SASE FEL intensity at a wavelength of ~60 nm.

The stabilization of the injector rf system leads to a small time jitter of the electron beam. We measured the arrival time jitter of the electron bunches with reference to the rf phase. The bunch arrival time was measured shot by shot using a cavity-type beam position monitor installed downstream of the C-band acceleration system. The measured time jitter was 46 fs in STD [30].

D. Replacement of second undulator magnetic array [31]

The second undulator had a large skew quadrupole component of 750 Gauss that rotated the beam profile downstream of the second undulator while closing the second undulator gap. A field correction was therefore carried out by sorting the permanent magnet blocks, whereas it could not recover the high field quality required for SASE FEL saturation. Although the reason for this insufficient field quality is still unclear, we guess that the cause is a difficulty in producing high-quality magnet blocks with the magnetization axes inclined to the magnet pole faces. Instead of the 45-deg inclined Halbach configuration, the conventional hybrid one was adopted for the new magnet array, which was installed at the beginning of September 2007. The skew quadrupole component of the new magnet array is 75 Gauss, being much lower than that of the old array (750 Gauss) and satisfying the multipole-error tolerance. The averaged pulse energy measured after replacement of the magnetic array has been found to be larger than that before by 1 order of magnitude. On the basis of this experience, we reinvestigated the undulator design for the 8-GeV XFEL source. We have subsequently changed the magnet configuration from the 45-deg inclined Halbach type to a hybrid one.

E. Precise orbit control in undulators [27]

The undulator magnetic field with a peak value of approximately 1 T has an effect of strong vertical focusing on the 250-MeV electron beam. In addition, the gap-dependent dipole error fields are not negligible. These error fields and the strong focusing cause serious orbit distortion over an undulator section. This distortion can degrade the laser intensity due to a reduced overlap between a laser

pulse and the electron beam through an undulator section. An orbit correction is thus necessary for each undulator gap.

The procedure to search for the optimum beam orbit is as follows. The beam orbit is tentatively set so that the orbit passes through the field center of each quadruple magnet at the upstream and the downstream locations of the undulators. The height of each undulator is then adjusted while fixing the undulator gap by using the laser intensity as a probe. Finally, the incidence orbit condition is mapped for each undulator so as to maximize the laser intensity.

F. Optimization of transverse beam envelope over undulators [27]

SASE FEL is produced from a small portion of a temporal slice in the electron bunch. Beam envelope optimization at the lasing slice is required to increase the amplification gain. However, it is generally difficult to adjust the slice envelope, which differs from the envelope averaged over the whole bunch. In particular, the difference is significant for the SCSS test accelerator with the velocity bunching system. There, a rather large chromatic phase shift of the betatron oscillation occurs over the bunch. We therefore cannot use the conventional monitors, such as the optical-transition-radiation monitor, which only provide the averaged profile. Although a transverse deflection cavity [32] directly provides the time-sliced profile, this system has not been installed in the SCSS test accelerator.

As an alternative method, we simply perform an iterative adjustment of beam-focusing parameters over the accelerator so as to maximize the laser intensity. Specific lenses and magnets, which were found to be highly sensitive to the laser intensity, are routinely used as knobs for beam envelope optimization. This has enabled us to increase the lasing intensity at the maximum by a few hundred percent. Note that a stable lasing condition is essential for performing both precise orbit setting and envelope optimization.

IV. ACHIEVED SASE FEL PERFORMANCE

After making the improvements and the fine beam tuning described in the previous section, the SASE FEL power has been remarkably enhanced. The simplest method to verify FEL saturation is a measurement of the gain curve, i.e., the radiation power, P, as a function of the undulator length, z. Within the framework of linear FEL theory [33], the dependence is given by

$$P = P_0 \exp\left(\frac{z}{L_g}\right), \tag{3}$$

where P_0 is the effective input power and L_g is the three-dimensional (3D) gain length [34]. The parameter z can be changed by opening gaps of several undulator segments or effectively by kicking out the electron beam with steering magnets. However, both methods are not applicable to the SCSS test accelerator; there are just two undulator segments, and it is difficult to generate a sufficiently strong magnetic field inside of an in-vacuum undulator.

Instead of z, we can change the gain length L_g by closing an undulator gap, and thus increasing the undulator deflecting parameter, K, and the radiation wavelength, λ. The relation between the two parameters, λ and K, is written by using λ_u as

$$\lambda = \frac{\lambda_u}{2\gamma^2}\left(1 + \frac{K^2}{2}\right). \tag{4}$$

Figure 9 [31] shows the inverse of the gain length plotted as a function of the wavelength and the undulator deflecting parameter. The assumed beam parameters for the calculation are given in the figure. These results indicate that the radiation power grows exponentially as the wavelength, and reaches saturation at a certain wavelength.

We measured the radiation pulse energy as a function of the wavelength. Figure 10 shows the measured pulse energy averaged over 30 shots as a function of the wavelength. In addition, the shot-by-shot fluctuation of the pulse energy (STD) is also plotted. The pulse energy increases exponentially in the wavelength region between 30 to 40 nm, while the growth rate drastically decreases in the wavelength region longer than 50 nm. The pulse energy fluctuation shows the evolution of a SASE process more clearly. At a wavelength of 30 nm, the fluctuation is less than 10%, which implies that the radiation process is spontaneous, and no laser amplification occurs. As the wavelength becomes longer, the fluctuation increases and reaches 50% at a wavelength of 40 nm. The SASE process

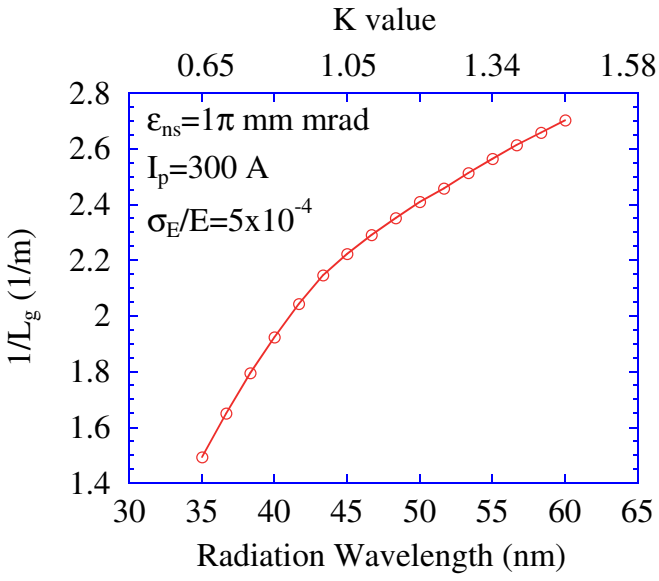

FIG. 9. (Color) Inverse of the 3D SASE gain length as a function of the wavelength. The undulator deflecting parameter, K, is indicated in the upper abscissa.

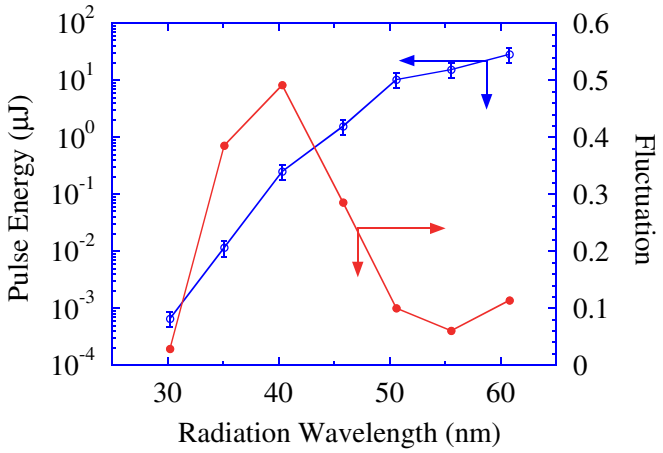

FIG. 10. (Color) Measured SASE pulse energy averaged over 30 shots and pulse-energy fluctuation (STD) as functions of the radiation wavelength. The error bar indicates the uncertainty (30%) for the pulse-energy calibration.

occurs in this wavelength region. As the wavelength increases from 40 to 50 nm, the fluctuation decreases immediately down to around 10%. From these results, we can conclude that the SASE process reaches saturation at a wavelength region longer than 50 nm [10,31].

We then measured the SASE FEL performance at two wavelengths, 50 and 60 nm. These wavelengths correspond to the minimum and the maximum in the wavelength region where the SASE saturation was observed. The long-term stability of SASE FEL was investigated. Once the beam parameter was tuned, the SASE saturation had continued at the two wavelengths until we intentionally terminated the beam operation. Figure 11 shows the shot-by-shot fluctuation of the pulse energy over 2 h at a wavelength of 50 nm with a repetition rate of 60 Hz. The fluctuation is ~11% in STD, including the drift of the pulse

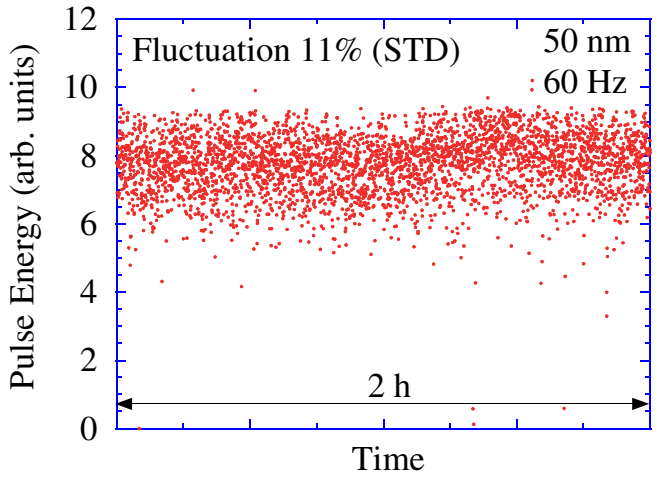

FIG. 11. (Color) Shot-by-shot fluctuation of the SASE pulse energy over a 2-h period at the wavelength of 50 nm with the repetition rate of 60 Hz.

TABLE II. Achieved FEL performance at SASE saturation.

Item	Achieved performance
Wavelength range	50–60 nm
Repetition rate	60 Hz
Pulse energy	~30 μJ@60 nm
Pulse-energy fluctuation	
30 shots	~10% (STD)
2 h	10%–12% (STD)
Laser size[a]	~3 mm (FWHM)
Pointing stability[a]	~5% to the beam size (STD)
Averaged spectrum width	0.6% (FWHM)

[a]Measurement point is ~10 m downstream from the source point.

energy over 2 h. This result is almost the same as the short-term fluctuation of 30 shots shown in Fig. 10, which proves that the accelerator system is sufficiently stable for SASE FEL operation in the EUV region. The achieved SASE FEL performance is summarized in Table II.

V. ESTIMATION OF NORMALIZED-SLICE EMITTANCE AT LASING PART

The achievement of SASE saturation in the SCSS test accelerator is an important step toward the realization of a compact SASE XFEL source. It should be noted, however, that the requirements on the beam parameters are more stringent for shorter wavelengths. It is thus important to quantitatively investigate the performances of the electron beam, particularly the sliced beam emittance (slice emittance), but not the projected one. The slice emittance can be measured directly by means of a transverse deflection cavity, which has not been installed in the SCSS test accelerator. Instead, we tried to evaluate the slice emittance by reproducing the measured dependence with a 3D FEL simulator. For this purpose, a temporal profile of the electron bunch was necessary.

A. Temporal profile of the electron bunch

The temporal profile of the electron bunch was measured by using the rf zero-phasing method [35]. Here, the electron bunch is linearly chirped with the second C-band acceleration unit, which is operated at the zero-crossing rf phase for beam acceleration. The temporal distribution is given by the energy spectrum observed at the dispersive chicane. Since the electron beam emittance provides a nonzero horizontal beam size, the measured spectrum is the convolution of a systematic energy chirp and the horizontal beam size. In order to reduce the contribution of the beam size to the measured spectrum, the strengths of the quadrupole triplet immediately upstream of the chicane were adjusted so as to minimize the horizontal beam size without introducing energy chirp. The ambiguity of the measurement comes from a beam energy measurement

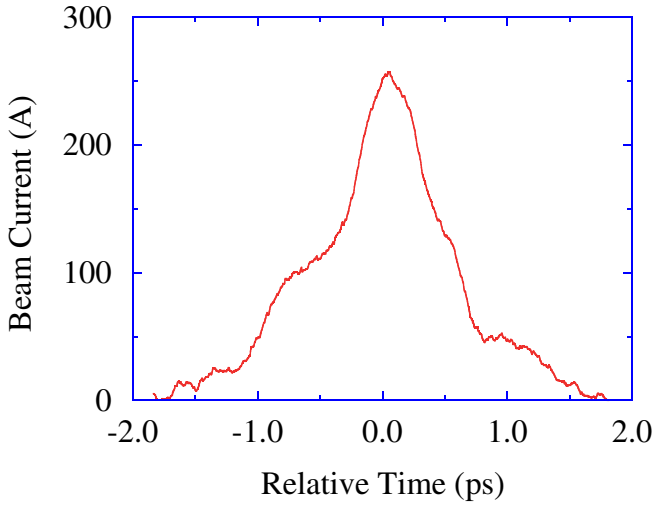

FIG. 12. (Color) Measured temporal distribution of the electron bunch.

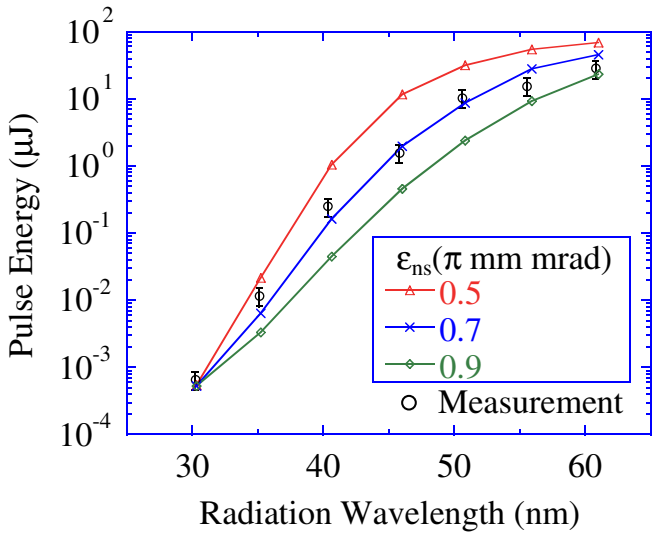

FIG. 13. (Color) Comparison of the measured pulse-energy dependence with that of the 3D SASE FEL simulations. Three values of the normalized-slice emittance (0.5π, 0.7π, and 0.9π mm mrad) were assumed. The error bar indicates the uncertainty (30%) for the pulse-energy calibration.

(uncertainty: ~5%), a scale calibration of the horizontal beam profile at the chicane (uncertainty: ~5%), and an unknown effect due to the intrinsic energy chirp (uncertainty: ~5%). The total uncertainty is estimated to be as low as 15%. Figure 12 shows the measured temporal distribution of the electron bunch, which was used for an emittance evaluation. The peak current and the peak width are approximately 300 A and 0.7 ps, respectively.

B. Evaluation of normalized-slice emittance with 3D FEL simulation code

With the measured temporal profile, FEL simulations were performed in order to reproduce the experimental results and to deduce the slice emittance. The 3D FEL simulation code SIMPLEX [36], developed at SPring-8, was used. The following three conditions were assumed: (i) The normalized-slice emittance, ϵ_{ns}, and the relative energy spread, σ_E/E, are maintained constant over the whole bunch, (ii) beam density distribution in the transverse phase space is bi-Gaussian, and (iii) σ_E/E is equal to 5×10^{-4}. Since the value of the slice energy spread was not experimentally measured in the test accelerator, it was assumed to be equal to the energy chirp over the slippage length in the simulation. Further discussion on the energy spread will be given in the following. The simulations for each experimental condition were repeated 30 times with different shot noise for SASE start-up in order to reproduce the experiments. Figure 13 shows the simulation results in terms of the pulse energy averaged over 30 sets at the undulator exit for three different values of ϵ_{ns}. It was found that FEL simulations with the parameter set $(\epsilon_{ns}, \sigma_E/E) = (0.7, 5 \times 10^{-4})$ well reproduce the experimental results [10,31].

Since the FEL gain length depends on both ϵ_{ns} and σ_E/E, it is impossible to uniquely determine the two parameters only by using simulations. Therefore, we investigated the distribution of the parameter set $(\epsilon_{ns}, \sigma_E/E)$, which can reproduce the experimental results. The gain length at a wavelength of 60 nm, calculated with the above-mentioned beam parameters by means of the universal scaling function [34], was found to be around 0.4 m. While keeping a gain length of 0.4 m, we calculated ϵ_{ns} as a function of σ_E/E, which is plotted in Fig. 14. The dashed line shows the value of ϵ_{ns} previously measured right after the electron gun by using the double-slit method [11]. Because ϵ_{ns} of the electron beam at the undulator entrance is definitely larger than this initial value, and the lower limit of σ_E/E is zero, the following conditions are

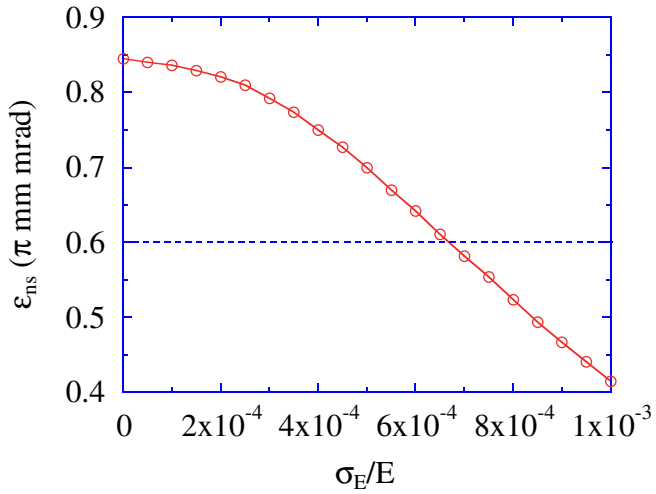

FIG. 14. (Color) Relation between ϵ_{ns} and σ_E/E to reproduce the experimental results.

concluded: (i) the relative energy spread σ_E/E is at least lower than 6×10^{-4}, and (ii) the normalized-slice emittance ϵ_{ns} is in between 0.6π and 0.8π mm mrad.

C. Comparisons between measurements and simulations for the SASE intensity fluctuation and spectrum characteristics

By using FEL simulations, we investigated whether the evaluated normalized-slice emittance ϵ_{ns} can reproduce the measured SASE intensity fluctuation and spectrum characteristics. The same electron beam parameters as in Sec. V B, $\epsilon_{ns} = 0.7\pi$ mm mrad and $\sigma_E/E = 5 \times 10^{-4}$, are used in the simulations. There are two sources of the SASE intensity fluctuation, a shot noise inherent in the SASE process and the peak current fluctuation of the electron beam due to the accelerator instability (8% in STD). The results of the simulation including these two sources are shown in Fig. 15 together with the measure fluctuation. We have found (i) the simulations explain the overall dependence of the SASE intensity fluctuation on the lasing wavelength, and (ii) the simulations, however, predict larger fluctuations than the measured ones in the SASE saturation range, especially from 50 to 55 nm. This discrepancy suggests that the gain length of the experiments is shorter than that obtained in the simulations. One possibility to interpret the measured shorter gain length is that the slice emittance of the electron beam may change with the location inside the bunch, while a constant emittance is assumed in the simulations.

The measured spectrum width at a wavelength of ~61 nm is 0.6% in FWHM, which is consistent with a simulation result of 0.8%. The measured number of SASE modes in the SASE saturation range is 5–10, which also agrees with the simulation result. Figure 16 shows examples of the measured and simulated single-shot spectrums.

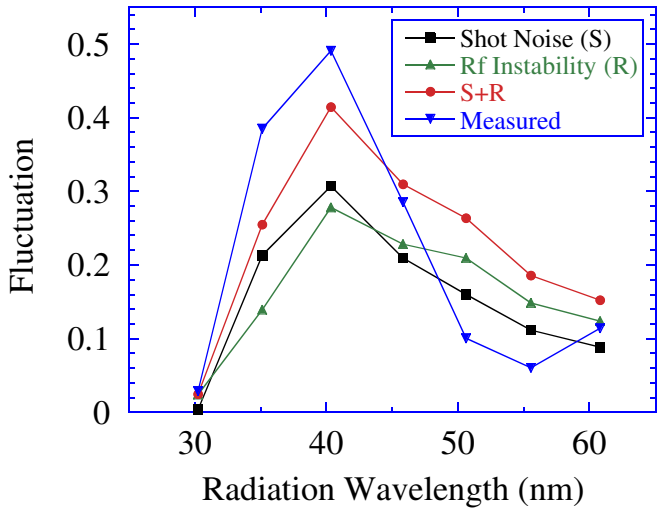

FIG. 15. (Color) Comparison of the measured fluctuation dependence with that of the 3D SASE FEL simulations. The black, green, and red symbols represent the simulated fluctuation dependences by shot noise (S), rf instability of the accelerator (R), and sum of S and R, respectively. The blue symbols represent the measured dependence.

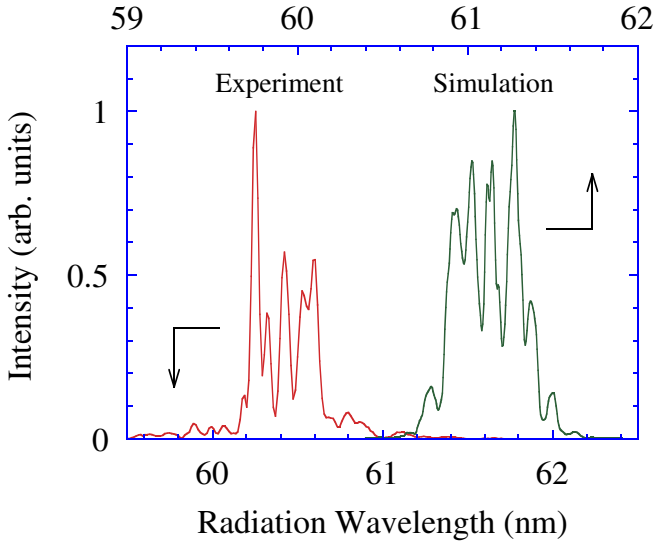

FIG. 16. (Color) Measured and simulated single-shot spectrums at around 61 nm.

VI. SUMMARY

The SCSS test accelerator was constructed in order to demonstrate the validity of the compact SASE source concept. SASE saturation was achieved for wavelengths ranging from 50 to 60 nm after improvements of the accelerator components and fine beam tuning. As a result of all these efforts, stable SASE saturation, which continues over the user experimental period, has finally been achieved. This stable operation has successfully provided photon beams to experimental users with the SASE FEL, which is characterized by a pulse energy of a few tens of μJ with a fluctuation of ~10% in STD.

A comparison between the experimental measurement and FEL simulation has deduced that the normalized-slice emittance at the lasing part is in between $\sim 0.6\pi$ and 0.8π mm mrad. This result shows that the normalized-slice emittance of the initial electron beam, 0.6π mm mrad in a 90% core part, is barely degraded by multistage bunch compression with a high compression factor of approximately 300. These results proved that the design concept of the SCSS test accelerator is applicable to the compact SASE XFEL source

ACKNOWLEDGMENTS

The authors would like to express their sincere gratitude to the staff of the SPring-8, particularly to S. Tanaka, Taichi Hasegawa, M. Oka, Y. Tajiri, and T. Morinaga for the machine operation of the SCSS test accelerator; K. Onoe, S. Kojima, S. Indo, and K. Nakashima for their technical

support; H. Tomizawa and T. Hatsui for their outstanding insights; and H. Suematsu and H. Ohno for their continuous encouragement. We would also like to thank H. Matsumoto and H. Baba for developing the C-band accelerator system.

[1] R. Bonifacio, C. Pellegrini, and L. M. Narducci, Opt. Commun. **50**, 373 (1984).
[2] K. Batchelor *et al.*, Nucl. Instrum. Methods Phys. Res., Sect. A **318**, 372 (1992).
[3] M. Altarelli *et al.*, Report No. DESY 2006-097, 2006.
[4] J. Arthur *et al.*, SLAC Report 593, 2002.
[5] T. Shintake, H. Matsumoto, T. Ishikawa, and H. Kitamura, in *Proceedings of SPIE, Optics for Fourth-Generation X-Ray Sources*, edited by R. Tatchyn, K. Freund, and T. Matsushita (SPIE, Bellingham, WA, 2001), Vol. 4500, pp. 12–23.
[6] SCSS X-FEL R&D Group, *SCSS X-FEL Conceptual Design Report*, edited by T. Shintake and T. Tanaka (RIKEN Harima Institute/SPring-8, Sayo, Japan, 2004).
[7] *SPring-8 Research Frontiers 2007*, edited by S. Kikuta (Japan Synchrotron Radiation Research Institute/SPring-8, Sayo, Japan, 2008), pp. 230–235.
[8] Y. Otake, in *Proceedings of FEL2008, Gyeongju, Korea, 2008* (Pohang Accelerator Laboratory, Pohang, Korea, 2009), pp. 222–226.
[9] H. Kitamura, Rev. Sci. Instrum. **66**, 2007 (1995).
[10] T. Shintake *et al.*, Nat. Photon. **2**, 555 (2008).
[11] K. Togawa, T. Shintake, T. Inagaki, K. Onoe, T. Tanaka, H. Baba, and H. Matsumoto, Phys. Rev. ST Accel. Beams **10**, 020703 (2007).
[12] D. L. Webster, J. Appl. Phys. **10**, 501 (1939).
[13] T. Shintake and SCSS Group, in *Proceedings of the 10th European Particle Accelerator Conference, Edinburgh, Scotland, 2006* (EPS-AG, Geneva, Switzerland, 2006), pp. 2741–2743.
[14] H. Tanaka *et al.*, in *Proceedings of FEL2006, Berlin, Germany, 2006* (BESSY, Berlin, Germany, 2006), pp. 769–776.
[15] T. Shintake, N. Akasaka, K. Bane, H. Hayano, K. Kubo, H. Matsumoto, S. Matsumoto, K. Oide, and K. Yokoya, in *Proceedings of the 1995 Particle Accelerator Conference, Dallas, Texas, 1995* (IEEE, Piscataway, NJ, 1996), pp. 1099–1101.
[16] K. Shirasawa, T. Inagaki, H. Kitamura, T. Shintake, S. Miura, H. Matsumoto, and H. Baba, in *Proceedings of the 2007 Particle Accelerator Conference, Albuquerque, New Mexico, 2007* (IEEE, Piscataway, NJ, 2007), pp. 2095–2097.
[17] T. Shintake, N. Akasaka, and H. Matsumoto, in *Proceedings of the 1997 Particle Accelerator Conference, Vancouver, British Columbia, 1997* (IEEE, Piscataway, NJ, 1998), pp. 455–457.
[18] Y. Ohkubo, H. Yonezawa, T. Shintake, H. Matsumoto, and N. Akasaka, in *Proceedings of the 19th Linear Accelerator Conference, Chicago, Illinois, 1998* (Argonne National Laboratory, Argonne, IL, 1998), pp. 2095–2097.
[19] T. Shintake, Jpn. J. Appl. Phys. **31**, L1567 (1992).
[20] T. Inagaki, in Proceedings of the 24th Linear Accelerator Conference, Victoria, British Columbia, 2008 (to be published).
[21] T. Tanaka, K. Shirasawa, T. Seike, and H. Kitamura, in *Proceedings of the 8th Conference on Synchrotron Radiation Instrumentation, San Francisco, California, 2003* (AIP, Woodbury, NY, 2004), pp. 228–230.
[22] M. Yabashi, T. Hirono, H. Kimura, H. Ohashi, S. Goto, S. Takahashi, K. Tamasaku, and T. Ishikawa, in Proceedings of FEL2006, Berlin, Germany, 2006 (Ref. [14]), pp. 785–792.
[23] http://www.uvsor.ims.ac.jp/eintroduction/page4.html.
[24] http://www.nist.gov/.
[25] T. Hara, H. Kitamura, T. Shintake, H. Tanaka, K. Togawa, and T. Tanikawa, in *Proceedings of APAC2007, Indore, India, 2007* (Raja Ramanna Centre for Advanced Technology, Indore, India, 2007), pp. 169–171.
[26] H. Maesaka, T. Shintake, Y. Otake, T. Hara, K. Togawa, T. Tanikawa, M. Yabashi, H. Tanaka, and SCSS Group, in *Proceedings of the 3rd Annual Meeting of Particle Accelerator Society of Japan, Sendai, Japan, 2006* (Tohoku University, Sendai, Japan, 2006), pp. 328–330, only title and abstract in English.
[27] H. Tanaka *et al.*, in *Proceedings of the 11th European Particle Accelerator Conference, Genoa, Italy, 2008* (EPS-AG, Geneva, Switzerland, 2008), pp. 1944–1946.
[28] S. Takahashi, T. Shintake, T. Saeki, K. Onoe, and T. Inagaki, in *Proceedings of APAC2004, Gyeongju, Korea, 2004* (Pohang Accelerator Laboratory, Pohang, Korea, 2005), pp. 678–680.
[29] H. Maesaka *et al.*, in Proceedings of the 11th European Particle Accelerator Conference, Genoa, Italy, 2008 (Ref. [27]), pp. 1404–1406.
[30] Y. Otake *et al.*, in *Proceedings of ICALEPCS2007, Knoxville, Tennessee, 2007* (SNS-ORNL, Knoxville, TN, 2007), pp. 706–710.
[31] T. Tanaka *et al.*, in Proceedings of FEL2008, Gyeongju, Korea, 2008 (Ref. [8]), pp. 537–542.
[32] O. H. Altenmueller, R. R. Larsen, and G. A. Loew, Rev. Sci. Instrum. **35**, 438 (1964).
[33] K.-J. Kim and M. Xie, Nucl. Instrum. Methods Phys. Res., Sect. A **331**, 359 (1993).
[34] M. Xie, in Proceedings of the 1995 Particle Accelerator Conference, Dallas, Texas, 1995 (Ref. [15]), pp. 183–185.
[35] D. X. Wang, G. A. Krafft, and C. K. Sinclair, Phys. Rev. E **57**, 2283 (1998).
[36] T. Tanaka, in *Proceedings of FEL2004, Trieste, Italy, 2004* (Sincrotrone Trieste, Trieste, Italy, 2004), pp. 435–438, http://radiant.harima.riken.go.jp/simplex/.